

# GENERALISABLE BIAS CORRECTION OF TWO-LINE ELEMENT SETS IN THE MEDIUM EARTH ORBIT REGIME

M. I. Hallgarten La Casta and D. Amato

*Imperial College London, London, SW7 2AZ, United Kingdom  
Email: m.hallgarten-la-casta21@imperial.ac.uk, d.amato@imperial.ac.uk*

## ABSTRACT

Two-line Element Sets (TLEs) remain, to this day, one of the few publicly-available, comprehensive sources of ephemerides for objects in the near-Earth environment. However, their intrinsic limited accuracy and effectively unknown uncertainty makes them unsuitable for precision applications, such as Conjunction Assessment (CA). Previous literature has shown that systemic, deterministic along-track errors are the primary source of error in TLEs. These along-track errors can be reduced with relatively simple models. In this study, it is shown that generalised models created with Global Navigation Satellite System (GNSS) data can reduce typical mean position errors by 40% while significantly suppressing oscillations affecting TLE-based Pseudo-Orbit Determination (P-OD).

Keywords: Orbit Determination; Two-Line Element Sets; Debiasing; Space Situational Awareness.

## 1. INTRODUCTION

The “New Space” era, driven by the growth in the number of commercial actors in the space domain, has led to a significant increase in the near-Earth Resident Space Object (RSO) population over the past decade, including year-on-year growth in the number of launches and payloads [1]. The majority of these RSOs are concentrated into the same limited regions, increasing the risk of collisions. This is driving the need for improving the capacity and capabilities of Conjunction Assessment (CA) systems.

Satellite operators remain dependent on governmental and commercial organisations, and data sharing with other operators, for Space Situational Awareness (SSA) data, such as state estimates for other satellites and objects. The financial cost of these services introduces a barrier which results in smaller operators and academia remaining reliant on publicly available sources, primarily Two-line Element Set (TLE) published by the United States Space Force (USSF).

TLEs have a number of advantages, including that they are freely available for a significant proportion of RSOs currently (and formerly) in near-Earth orbit, and that the analytical model used for propagation (SGP4 and SDP4, commonly referred to jointly as SGP4) has a very low computational cost. These advantages result in an ability to generate a large number of RSO state vectors quickly and cheaply. Nevertheless, the intrinsic limited accuracy and effectively unknown uncertainty of TLEs, make them unsuitable for precision applications, such as CA.

The development of SGP4-XP seeks to address some of these limitations [2–4], however the compatible Type 4 TLEs still remain to be published routinely, leaving the SSA community reliant on traditional TLEs. Additionally, it is unclear whether the historical catalogue will be updated to include Type 4 TLEs.

Previous literature has demonstrated that Pseudo-Orbit Determination (P-OD) on TLEs can produce more accurate state estimates [5–7]. In this process, TLEs are propagated with SGP4 to produce pseudo-observations of the objects which are fed into well known state estimation algorithms. Nevertheless, systemic, deterministic biases are present in the TLE dataset [8, 9] which can significantly degrade the accuracy of P-OD techniques. Compensating for these biases poses a critical challenge for improving state estimation with TLE-based pseudo-observations [10].

Along-track error is the primary source of error in TLEs [6]. The along-track error present in TLE-based state predictions varies significantly for objects with periods above 225 minutes, where deep-space terms are included in SGP4 [11]. This corresponds primarily to objects in Medium Earth Orbit (MEO) and Geostationary Earth Orbit (GEO) where previous analysis has found systematic along-track errors with periods of approximately one month [10].

The presence of biases presents an issue for instantaneous TLE accuracy, but even more so when conducting P-OD: fits based on TLE pseudo-observations can be heavily skewed by biases. In some cases, this can result in state estimates, which when propagated into the future, have position accuracies which are worse than simply propagating the original TLEs with SGP4.

In Section 2, the methodology for creating bias models will be described, followed in Sections 3 and 4 by several examples of data-driven models which can be used to debias TLE pseudo-observations in MEO. The performance of these models is investigated in Section 5, before concluding in Section 6.

## 2. MODELLING TLE ERRORS

Reference states are generated from Standard Product 3 (SP3) files, produced from either Satellite Laser Ranging (SLR) or Global Navigation Satellite System (GNSS) pseudo-ranging. These reference states are compared against the predicted states from TLEs to calculate the state errors, and hence bias, present in the TLE catalogue. Bias models are then created based on the state errors between the TLEs and SP3 data. Following the creation of the models, they are evaluated to determine their quality and performance. This is achieved by comparing the debiased TLE states against the SP3 states to measure any reductions in state error.

A summary of the model creation process is presented in Fig. 1, highlighting the generation of states from TLEs and SP3 files to calculate the bias.

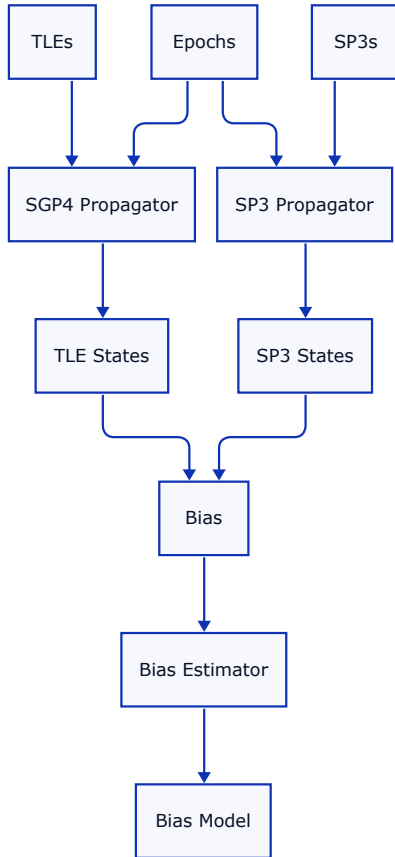


Fig. 1. Flowchart of the bias model creation process.

The satellites considered for the study are presented in Table 1, including several Galileo and Global Positioning System (GPS) satellites, and the LAGEOS and Etalon geodesy satellites.

Table 1. Satellites considered during the study.

Name	NORAD ID	SP3/PRN
GALILEO 16 (26C)	41860	E03
GALILEO 18 (26E)	41862	E05
GALILEO-FM2	37847	E12
GALILEO 24 (2C0)	43567	E13
GALILEO 25 (2C1)	43564	E15
GALILEO 5 (261)	40128	E18
GALILEO 20 (2C6)	43056	E25
GALILEO 7 (263)	40544	E26
GALILEO 21 (2C7)	43057	E27
GALILEO 10 (206)	40890	E30
GALILEO 22 (2C8)	43058	E31
GALILEO 26 (2C2)	43565	E33
GALILEO 23 (2C9)	43566	E36
NAVSTAR 66 (USA 232)	37753	G01
NAVSTAR 56 (USA 180)	28474	G02
NAVSTAR 72 (USA 258)	40294	G03
NAVSTAR 77 (USA 289)	43873	G04
NAVSTAR 64 (USA 206)	35752	G05
NAVSTAR 70 (USA 251)	39741	G06
NAVSTAR 62 (USA 201)	32711	G07
NAVSTAR 74 (USA 262)	40730	G08
NAVSTAR 71 (USA 256)	40105	G09
NAVSTAR 75 (USA 265)	41019	G10
NAVSTAR 81 (USA 319)	48859	G11
NAVSTAR 59 (USA 192)	29601	G12
NAVSTAR 43 (USA 132)	24876	G13
NAVSTAR 80 (USA 309)	46826	G14
NAVSTAR 60 (USA 196)	32260	G15
NAVSTAR 51 (USA 166)	27663	G16
NAVSTAR 57 (USA 183)	28874	G17
NAVSTAR 78 (USA 293)	44506	G18
NAVSTAR 54 (USA 177)	28190	G19
NAVSTAR 52 (USA 168)	27704	G21
NAVSTAR 67 (USA 239)	38833	G24
NAVSTAR 65 (USA 213)	36585	G25
NAVSTAR 73 (USA 260)	40534	G26
NAVSTAR 68 (USA 242)	39166	G27
NAVSTAR 61 (USA 199)	32384	G29
NAVSTAR 69 (USA 248)	39533	G30
NAVSTAR 58 (USA 190)	29486	G31
NAVSTAR 76 (USA 266)	41328	G32
LAGEOS-1	8820	L51
LAGEOS-2	12160	L52
Etalon 1	19751	L53
Etalon 2	20226	L54

### 2.1. Datasets

#### 2.1.1. Two-line Element Sets

TLEs are provided by USSF via Space-Track<sup>1</sup>. For the satellites considered in this analysis, TLEs are released approximately every one or two days. In some cases TLEs can be re-issued to update parameters, creating scenarios where, for a given epoch, multiple TLEs exist for a single object. To avoid this ambiguity, the most recently released TLE is used as it represents the most up-to-date information.

<sup>1</sup>Available at: <https://space-track.org/> (accessed on 10/03/2025)

Object states are represented in TLEs by a number of parameters, including a set of mean elements, based on a development from theories by Brouwer and Kozai, among others [11, 12], and a ballistic coefficient. Propagation of these parameters to future times, and conversion to Cartesian state, is based on the SGP4 single-averaged theory. For orbits with a period greater than 225 minutes, deep space perturbations are included to “account for lunar and solar gravitation as well as the resonance effects of Earth tesseral harmonics” [11].

Propagation with SGP4 can be expressed analytically as:

$$\mathbf{y}(t) = \mathbf{R}_{\text{TEME}}(t) \mathbf{g}(\mathbf{z}_k, t), \quad (1)$$

$$\mathbf{z}(t_k) = \mathbf{z}_k, \quad (2)$$

where  $\mathbf{y}(t)$  is the TLE-based osculating Cartesian state in the Geocentric Celestial Reference Frame (GCRF) at a future time  $t$ ;  $\mathbf{R}_{\text{TEME}}(t)$  is the transformation matrix which rotates from the True Equator Mean Equinox (TEME) frame to the GCRF;  $\mathbf{g}(\mathbf{z}, t)$  represents the mapping in SGP4 from the TLE state to the osculating TEME Cartesian state; and  $t_k$  and  $\mathbf{z}_k$  are the epoch and state of the appropriate TLE respectively, including both the mean elements and ballistic coefficient.

The TLE sampling strategy proposed for P-OD by Levit and Marshall [5] was used to generate pseudo-observations. Sampling times were equally spaced between the start and end epochs of the evaluation window. The state at given time was calculated by propagating the most recent preceding TLE forward in time with SGP4. For sample times before the first TLE, states were calculated by propagating backwards in time.

SGP4 conducts propagation in its set of mean elements which are converted then into Cartesian positions and velocities in TEME. These are transformed into GCRF for consistency with the SP3-based states. In this work, both the SGP4 propagation and frame transformations were provided by the Orekit spacecraft library [13].

### 2.1.2. Standard Product 3 Data

“Ground truth” data in the form of post-processed, high-accuracy ephemerides was provided through NASA’s Crustal Dynamics Data Information System (CDDIS), both for LAGEOS-1 and -2, and Etalon 1 and 2, based on SLR<sup>2</sup>; and for Galileo and GPS satellites, based on GNSS pseudo-ranging<sup>3</sup>.

The SLR- and GNSS-based data is provided in the form of post-processed orbit products using the SP3 format.

<sup>2</sup>Available at: <https://cddis.nasa.gov/archive/slr/products/orbits/> (accessed on 10/03/2025)

<sup>3</sup>Available at: <https://cddis.nasa.gov/archive/gnss/products/> (accessed on 10/03/2025)

This format includes state vectors at a series of epochs for each satellite, each identified by a SP3 identifier. For GNSS satellites, this identifier is based on the Pseudo-Random Noise (PRN) codes, in this case with the prefixes “E” and “G” for Galileo and GPS, respectively.

Interpolation between the state vectors at each epoch is conducted to generate satellite states for any given time within the timespan of the SP3 data. In the case of the GNSS satellites, velocities were not included in the SP3 files, therefore these were estimated as part of the interpolation process. Both the SP3 interpolation and frame transformations were provided by the Orekit spacecraft library [13].

## 2.2. Along-track Error

The position error is simply the difference between the positions from the TLEs and SP3:

$$\Delta \mathbf{r}(t) = \mathbf{r}_{\text{TLE}}(t) - \mathbf{r}_{\text{SP3}}(t). \quad (3)$$

The along-track position error can be extracted from the Radial, Transverse, Normal (RTN) position error, found by rotating the position error vector into to an RTN frame:

$$\Delta \hat{\mathbf{r}}(t) = \mathbf{R}_{\text{RTN}}(\mathbf{r}_{\text{TLE}}(t)) \Delta \mathbf{r}(t), \quad (4)$$

where  $\mathbf{R}_{\text{RTN}}(\mathbf{r}_{\text{TLE}}(t))$  is the transformation matrix which rotates the position error from the GCRF to RTN frame, based on position vector from the TLE.

The along-track angular error is calculated by dividing the along-track position error by the the magnitude of the radial distance of the object:

$$\Delta \theta_T(t) = \frac{\Delta \hat{r}_T(t)}{\|\mathbf{r}_{\text{TLE}}(t)\|}. \quad (5)$$

where  $\Delta \hat{r}_T(t)$  is the along-track component of the position error.

## 2.3. Model Fitting

The along-track error is modelled using a scalar function:

$$\Delta \theta_T^*(\mathbf{u}) = f(\mathbf{u}, \boldsymbol{\mu}), \quad (6)$$

where  $\mathbf{u}$  are a set of inputs, such as time or parameters of a perturbing acceleration, and  $\boldsymbol{\mu}$  are the model parameters.

The model can be linearised with respect to the model parameters for a given set of inputs:

$$\Delta\theta_T^*(\mathbf{u}) = \mathbf{A}(\mathbf{u})\boldsymbol{\mu}, \quad (7)$$

where  $\mathbf{A}(\mathbf{u})$  is a partial derivatives matrix that maps the model parameters to the estimated along-track error.

The individual linear systems can be concatenated into a single overall linear system which maps the model parameters to a set of estimated along-track errors:

$$\begin{bmatrix} \Delta\theta_{T,0}^* \\ \Delta\theta_{T,1}^* \\ \vdots \\ \Delta\theta_{T,n-1}^* \end{bmatrix} = \begin{bmatrix} \mathbf{A}_0 \\ \mathbf{A}_1 \\ \vdots \\ \mathbf{A}_{n-1} \end{bmatrix} \boldsymbol{\mu}, \quad (8)$$

where each  $\Delta\theta_{T,i}^*$  corresponds to the along-track error at a given epoch and for a given object. Sets of along-track errors belonging to different objects can be also concatenated in a single along-track error vector through equation (8). The predicted along-track errors can be expressed as a function of an overall derivatives matrix and the parameters of the bias model:

$$\Delta\theta_T^* = \mathbf{H}\boldsymbol{\mu}, \quad (9)$$

The errors between the actual and predicted along-track errors are expressed as a set of residuals:

$$\mathbf{b} = \Delta\theta_T - \Delta\theta_T^*, \quad (10)$$

$$= \Delta\theta_T - \mathbf{H}\boldsymbol{\mu}. \quad (11)$$

The process of fitting the model parameters to the along-track errors is expressed as an optimisation problem with the objective of minimising the sum of the square of the residuals:

$$\min_{\boldsymbol{\mu}} J(\boldsymbol{\mu}) = \frac{1}{2} \mathbf{b}^T \mathbf{b}, \quad (12)$$

$$= \frac{1}{2} (\Delta\theta_T - \mathbf{H}\boldsymbol{\mu})^T (\Delta\theta_T - \mathbf{H}\boldsymbol{\mu}), \quad (13)$$

where  $J(\boldsymbol{\mu})$  is the objective function.

It can be shown that the minimisation problem can be expressed as the solution to a linear system [14, 15], known as the Gauss-Newton method:

$$(\mathbf{H}_i^T \mathbf{H}_i) \delta\boldsymbol{\mu}_i = \mathbf{H}_i^T \mathbf{b}_i, \quad (14)$$

$$\boldsymbol{\mu}_{i+1} = \boldsymbol{\mu}_i + \delta\boldsymbol{\mu}_i, \quad (15)$$

where  $\delta\boldsymbol{\mu}_i$  is the best estimate of the optimal decision vector update for the  $i$ -th iteration. Due to the non-linearity of the models, the minimisation is iterated by re-linearising at each solution. This iteration continues until convergence is reached.

For this study, an enhanced version of the Gauss-Newton method was used: the Levenberg-Marquardt method [16, 17]. This method adaptively updates the solution by introducing a gradient descent term into the update equation:

$$[\mathbf{H}_i^T \mathbf{H}_i + \lambda \text{diag}(\mathbf{H}_i^T \mathbf{H}_i)] \delta\boldsymbol{\mu}_i = \mathbf{H}_i^T \mathbf{b}_i, \quad (16)$$

where  $\lambda$  is the damping coefficient, which determines the importance of the gradient descent update (the second term in brackets in Eq. (16)) relative to the Gauss-Newton update. The method initially prioritises gradient descent. The damping coefficient is reduced during iteration to increase the influence of the Gauss-Newton solution as the solver approaches the local minimum.

## 2.4. Model Evaluation

Models were evaluated by considering the position errors following debiasing (i.e. the application of the bias model to the states):

$$\Delta r_i = \|\mathbf{r}_i^* - \mathbf{r}_i\|, \quad (17)$$

where  $\mathbf{r}_i^*$  and  $\mathbf{r}_i$  are the predicted and true positions, respectively, at the  $i$ -th epoch.

The position Root-Mean-Square Error (RMSE) was used as the primary metric for model quality when considering an entire set of predictions:

$$\Delta r_{\text{RMSE}} = \sqrt{\frac{1}{n} \sum_i^n \Delta r_i^2}, \quad (18)$$

where  $n$  is the number of samples.

Additional metrics considered include the mean and standard deviation of the position errors:

$$\overline{\Delta r} = \frac{1}{n} \sum_i^n \Delta r_i, \quad (19)$$

$$\sigma_{\Delta r} = \sqrt{\frac{1}{n} \sum_i^n (\Delta r_i - \overline{\Delta r})^2}. \quad (20)$$

### 3. BIAS MODELS

#### 3.1. Time-based Model

A simple model for estimating the along-track biases considers a sinusoidal behaviour with respect to time [10]:

$$\Delta\theta_T(t) \approx a_t \sin\left[\frac{2\pi}{b_t}(t + c_t)\right] + d_t, \quad (21)$$

where  $t$  is time, expressed in days since 1<sup>st</sup> January 2000 at 12:00 Terrestrial Time (TT)<sup>4</sup>; and  $a_t$ ,  $b_t$ ,  $c_t$ , and  $d_t$  are model parameters, corresponding to the amplitude, period, phase, and offset of the oscillation, respectively.

The time-based model was fit individually to the geodesy satellites and the GNSS satellites. The models for the geodesy satellites are presented in Fig. 2 and Table 2. The model showed good agreement with the along-track errors of Etalon 1 and 2, and limited agreement for LAGEOS-1, where an additional longer-term variation was present. LAGEOS-2's model had a complete lack of agreement due to the satellite's along-track error exhibiting a significant different behaviour with large variations in amplitude.

Table 2. Individual time-based model parameters.

Satellite	$a_t$ [rad]	$b_t$ [days]	$c_t$ [days]	$d_t$ [rad]
LAGEOS-1	$1.42 \times 10^{-5}$	27.5	-1.1	$1.32 \times 10^{-7}$
LAGEOS-2	$2.40 \times 10^{-6}$	26.1	-8.9	$-4.01 \times 10^{-6}$
Etalon 1	$4.83 \times 10^{-5}$	27.5	-2.8	$-4.66 \times 10^{-7}$
Etalon 2	$6.76 \times 10^{-5}$	27.6	-13.4	$2.71 \times 10^{-7}$

One notable feature of the models was their periods. These had close alignment with the Moon's sidereal orbital period of approximately 27.3 days, supporting the suggestion that errors in modelling lunar perturbations in SGP4 contributes to the along-track error [10].

The models for Etalon 1 and 2 were roughly in phase with each other throughout the year 2022, despite the difference in phase in the model. The slight difference in period between the two models meant that there was a small amount of drift. This drift, accumulated over a 22 year timespan, resulted in a significant phase difference when defining the model at J2000.

#### 3.2. Moon-based Model

An alternative formulation, based on the position of the Moon along its orbit, more directly considers the position-based nature of the perturbation mismatching [10]:

<sup>4</sup>The reference epoch has been changed from a previous study [10] to more closely align with the commonly used J2000 epoch.

$$\Delta\theta_T(M) \approx a_m \sin(M + c_m) + d_m, \quad (22)$$

where  $M$  is the mean anomaly of the Moon; and  $a_m$ ,  $c_m$ , and  $d_m$  are model parameters.

The fitted Moon-based models for the geodesy satellites are presented in Fig. 3 and Table 3. The model showed good agreement with the along-track errors of LAGEOS-1, and Etalon 1 and 2. The additional longer-term variation for LAGEOS-1 was not visible when plotted as a function of the Moon's mean anomaly. In a similar fashion as the time-based model, LAGEOS-2's Moon-based model was unable to capture the variation in along-track error throughout the year.

Table 3. Individual Moon-based model parameters.

Satellite	$a_m$ [rad]	$c_m$ [rad]	$d_m$ [rad]
LAGEOS-1	$1.33 \times 10^{-5}$	$1.73 \times 10^{-1}$	$1.63 \times 10^{-7}$
LAGEOS-2	$1.96 \times 10^{-6}$	$-3.42 \times 10^{-1}$	$-4.05 \times 10^{-6}$
Etalon 1	$4.62 \times 10^{-5}$	$-8.42 \times 10^{-2}$	$-6.24 \times 10^{-7}$
Etalon 2	$6.59 \times 10^{-5}$	$1.00 \times 10^{-2}$	$1.09 \times 10^{-7}$

#### 3.3. General Moon-based Model Behaviours

The individual fits of the Moon-based model on the GNSS satellites are presented in Fig. 4 to investigate correlations between the model parameters and a subset of Keplerian orbital elements.

There appeared to be generally limited correlation between the Keplerian orbital elements and the model parameters. An exception was the amplitudes of the model and the mean Right Ascension of the Ascending Node (RAAN) of each satellite which, bar some outliers, appeared to have a strong correlation, suggesting that a further development of the time- and Moon-based models could consider the RAAN of the satellite.

The phases for all of the models remained near-zero with a largest absolute departure from zero of approximately 0.22 rad (or 12.6°). The impact of the Moon on the bias, therefore, is near-zero when the Moon is near its perigee and apogee, consistently for all of the satellites. It should be noted that the distribution of the phases is different for the two constellations: the Galileo phases were typically greater than zero, while the GPS phases were more centred about zero.

A significant difference in behaviour between Galileo and GPS can be seen in the offsets: the fits on Galileo satellites had a constant near-zero offset; while the fits on GPS satellites had much more variance, mainly in a band from  $-2 \times 10^{-4}$  to  $2 \times 10^{-4}$  rad. The GPS TLEs often have a mean along-track shift, either leading or lagging the true position of the satellite, which does not appear correlated with any of the Keplerian orbital elements.

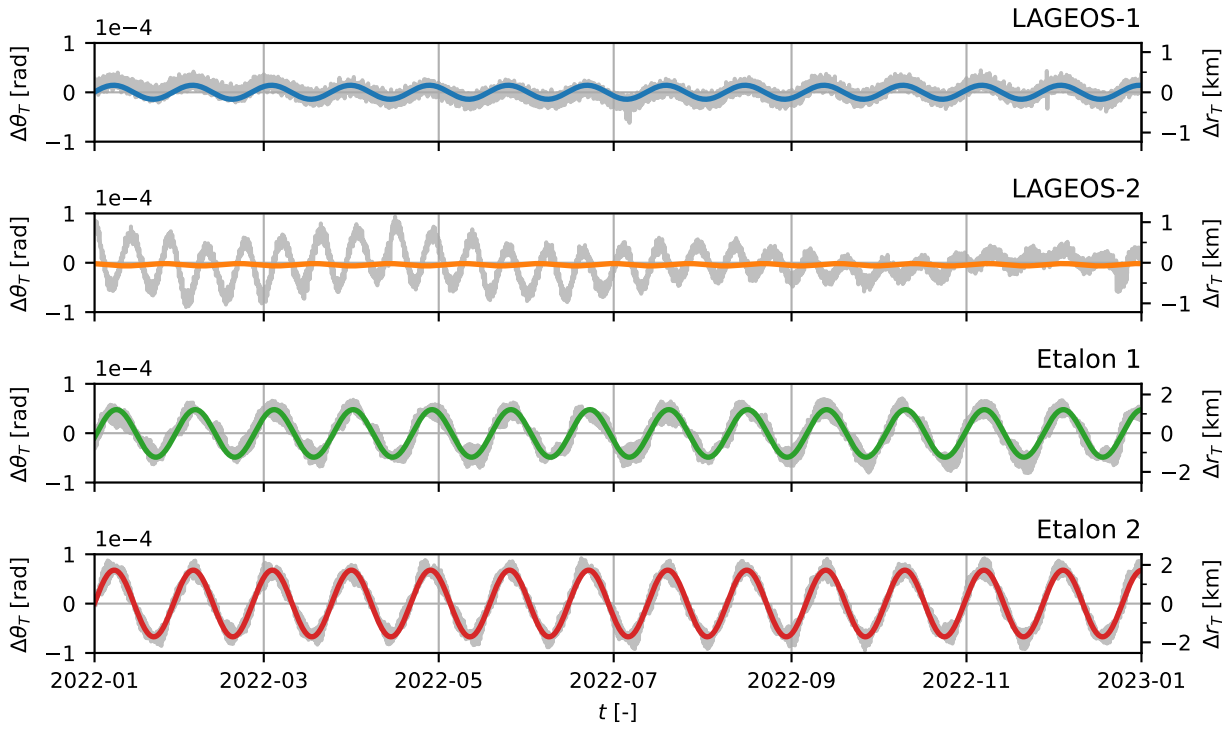


Fig. 2. Along-track errors of TLEs with respect to SLR as a function of time. The SLR data and individual time-based models are presented in grey and colour respectively.

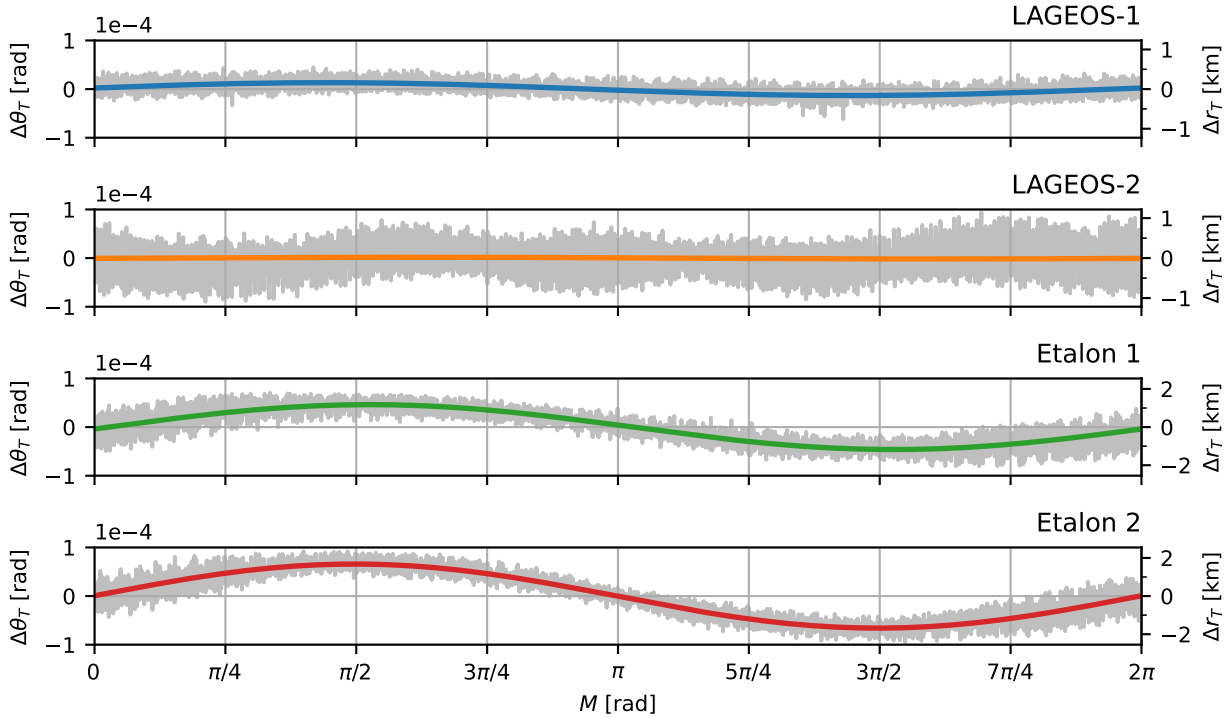


Fig. 3. Along-track errors of TLEs with respect to SLR as a function of Moon mean anomaly. The SLR data and individual Moon-based models are presented in grey and colour respectively.

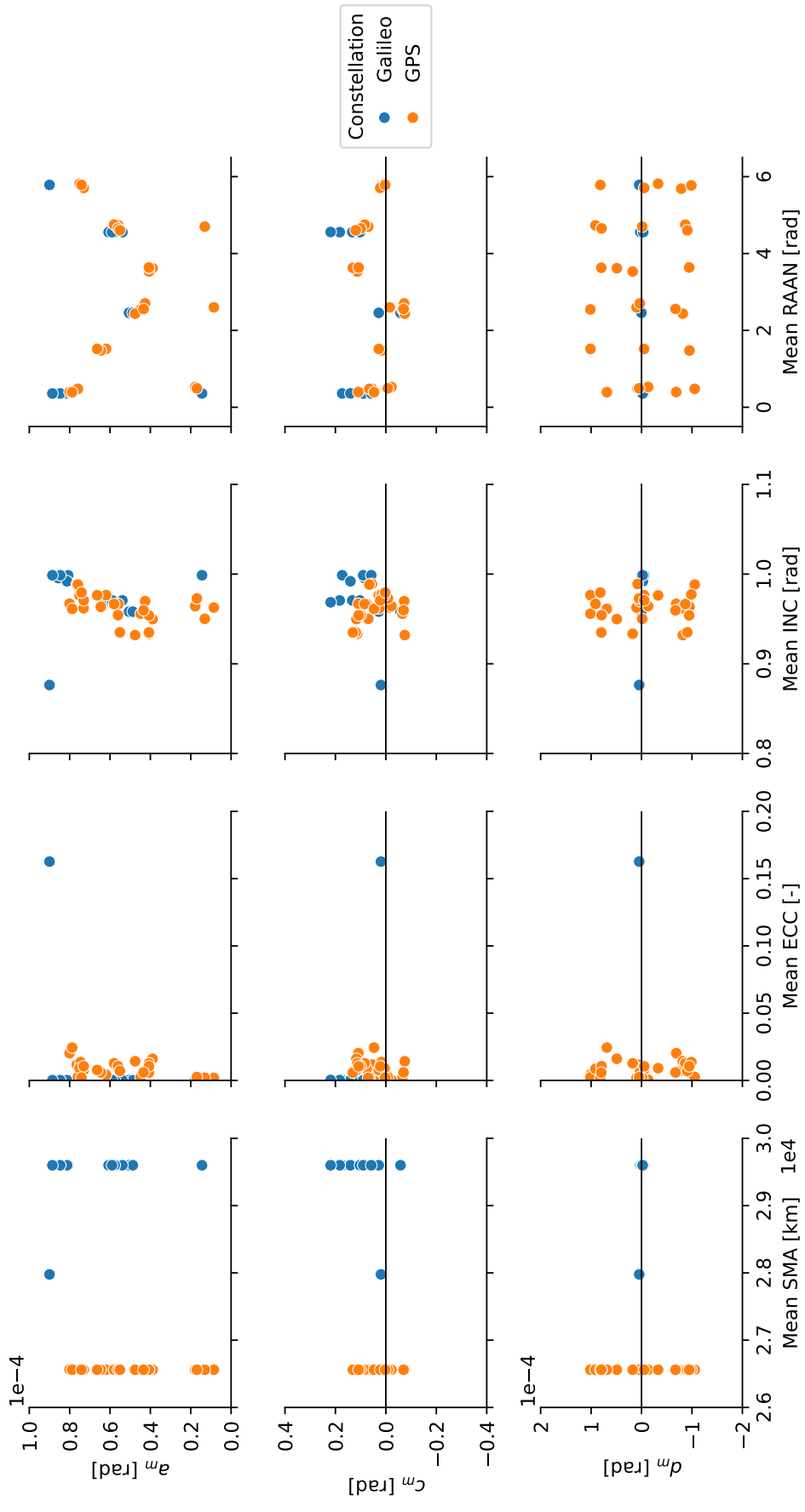


Fig. 4. Moon-based model parameters for individual fits on a selected set of GNSS satellites, as function of the mean of each satellite's osculating Keplerian elements throughout the year 2022.

The relationship between the RAAN of the satellites and the amplitude of their respective Moon-based models was approximated with an additional sine function:

$$a(\Omega) \approx \alpha \sin(\Omega + \beta) + \gamma, \quad (23)$$

where  $\Omega$  is the RAAN of the satellite, and  $\alpha$ ,  $\beta$ ,  $\gamma$  are model parameters.

In five cases (one Galileo and four GPS) the amplitudes of the individual Moon-based models did not appear to follow the sinusoidal behaviour with respect to RAAN, therefore these cases, all with amplitudes below  $0.2 \times 10^{-4}$  rad, were excluded from the fitting procedure.

It should be noted that the fit illustrated in Table 4 and Fig. 5 was based on the mean osculating RAAN of each satellite throughout the year. This element cannot be assumed to remain constant with respect to time, due to influences such as nodal precession and manoeuvres, therefore this example provides an initial guess for the parameters needed to capture the effect of RAAN with a more detailed model.

Table 4. RAAN-based amplitude model parameters, derived from individual fits with Eq. (22).

$\alpha$	$2.08 \times 10^{-5}$	rad
$\beta$	1.44	rad
$\gamma$	$6.10 \times 10^{-5}$	rad

One interesting result of fitting the RAAN-based amplitude model was the model's phase of 1.44 rad (or  $82.5^\circ$ ). During the year 2022, the Moon's RAAN in GCRF ranged from  $7.33$  to  $10.3^\circ$  with a mean value of  $8.60^\circ$ . This suggests that the phase of the amplitude model could be tied directly to the difference between the RAANs of each satellite and the Moon.

### 3.4. Combined Models

The combined versions of the time- and Moon-based models presented in Eqs. (21) and (22) replace constant amplitude with the RAAN-based relationship in Eq. (23):

$$\Delta\theta_T(t, \Omega) \approx a_t(\Omega) \sin\left[\frac{2\pi}{b_t}(t + c_t)\right] + d_t, \quad (24)$$

$$\Delta\theta_T(M, \Omega) \approx a_m(\Omega) \sin(M + c_m) + d_m. \quad (25)$$

For each combined model, a single set of model parameters was estimated using all of the GNSS satellite residuals concatenated together, excluding the outlying cases. The model parameters resulting from fitting the full combined models are presented in Table 5.

Table 5. Combined model parameters.

(a) Time-based.		
$b_t$	$2.76 \times 10^1$	days
$c_t$	$1.07 \times 10^1$	days
$d_t$	$-6.58 \times 10^{-6}$	rad
$\alpha_t$	$2.06 \times 10^{-5}$	rad
$\beta_t$	1.44	rad
$\gamma_t$	$6.28 \times 10^{-5}$	rad
(b) Moon-based.		
$c_m$	$5.99 \times 10^{-2}$	rad
$d_m$	$-6.64 \times 10^{-6}$	rad
$\alpha_m$	$2.08 \times 10^{-5}$	rad
$\beta_m$	1.44	rad
$\gamma_m$	$6.09 \times 10^{-5}$	rad

## 4. DYNAMIC MODE DECOMPOSITION

Dynamic Mode Decomposition (DMD) is a linear dimensionality reduction technique which models time-series data as a linear dynamical system [18–21]:

$$\mathbf{x}(t_{k+1}) \approx \mathbf{A}\mathbf{x}(t_k). \quad (26)$$

The linear system can be expressed with two time-shifted matrices of a given set of observed states:

$$\mathbf{X}_1 = \begin{bmatrix} | & | & \dots & | \\ \mathbf{x}(t_1) & \mathbf{x}(t_2) & \dots & \mathbf{x}(t_{n-1}) \\ | & | & & | \end{bmatrix}, \quad (27)$$

$$\mathbf{X}_2 = \begin{bmatrix} | & | & \dots & | \\ \mathbf{x}(t_2) & \mathbf{x}(t_3) & \dots & \mathbf{x}(t_n) \\ | & | & & | \end{bmatrix}, \quad (28)$$

$$\mathbf{X}_2 \approx \mathbf{A}\mathbf{X}_1. \quad (29)$$

In traditional DMD, a solution can be found through the Moore-Penrose pseudo-inverse [18], however several alternative algorithms exist. One of the limitations of traditional DMD is that it is highly sensitive to noise. This led to the development of Optimised Dynamic Mode Decomposition (OptDMD) [22], and later Bagging, Optimised Dynamic Mode Decomposition (BOP-DMD) [23]. These versions of DMD provide greater resilience to noise through the use of numerical optimisation techniques. Furthermore, several features were introduced which improved the adaptability of the method for modelling different dynamics, such as the ability to specify constraints on the eigenvectors of the system.

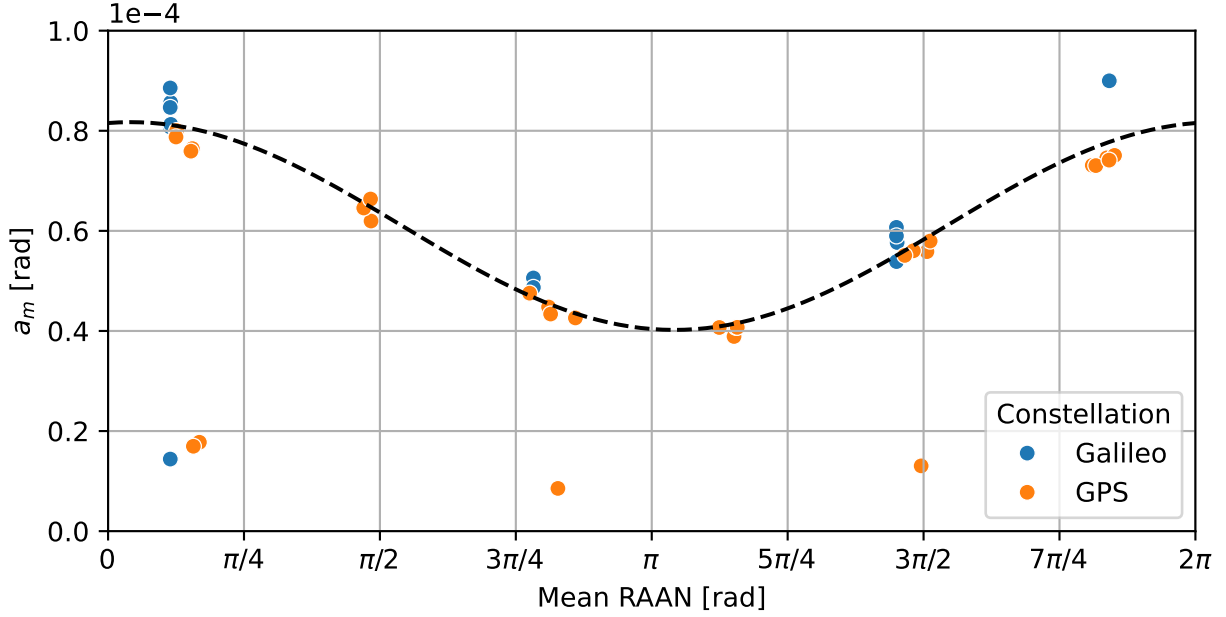


Fig. 5. Individual Moon-based model amplitudes as a function of the mean of each satellite’s osculating Keplerian elements throughout the year 2022. The dashed line represents the fitted amplitude model.

Time-delay embedding, in the form of Hankel preprocessing, was used to augment the state space [21] before conducting OptDMD fits. The method augments the state space by stacking states from several successive times together, increasing the dimensionality of the system.

The results of testing traditional DMD, OptDMD, and OptDMD with Hankel preprocessing are presented in Fig. 6. For both Etalon 1 and 2, traditional DMD failed to capture the oscillatory behaviour of the along-track error, as expected due to the high amount of noise. Likewise, stand-alone OptDMD did not successfully model this behaviour. OptDMD with Hankel preprocessing, on the other hand, successfully converged on a solution similar to the time-based model of a single sinusoidal variation throughout the year. In the case of Etalon 2, it can be seen by visual inspection that the frequency of the model does not match the underlying observations.

Despite OptDMD’s greater resilience to noise in the observations, it was found, in some cases, that the combination of noise and specific hyperparameters prevented the solver from converging on a solution. A significant amount of manual trial and error was required to find successful hyperparameters.

Smoothing the signal with a moving average of several days was found to improve the robustness of the method. Nevertheless, this removed high-frequency information which could be used otherwise in a more detailed model. Additionally, convergence was still sensitive occasionally to the size of the averaging window, suggesting that this strategy was not without issues.

## 5. COMBINED MODEL PERFORMANCE

### 5.1. Geodesy Satellites

The results of applying the combined time- and Moon-based models to the geodesy satellites are presented in Figs. 7 and 8 respectively. In the cases of LAGEOS-1 and -2, both of the combined models failed to accurately estimate the along-track error. Conversely, the combined models accurately modelled the along-track errors for Etalon 1 and 2, albeit not as accurately as their corresponding individual models.

In the case of LAGEOS-1, the amplitudes were overestimated by up to almost three times. The use of these models would degrade P-OD significantly due to the introduction of oscillations larger than present in the TLEs. One interesting result can be seen by the change in amplitudes, decreasing in the case of LAGEOS-1 and increasing in the case of LAGEOS-2, highlighting the change in RAAN for both satellites. In the case of LAGEOS-2, the change in model amplitude is opposite to actual change in amplitude in its TLEs.

The combined models produced generally good bias estimates for Etalon 1 and 2, matching the true along-track errors. Nevertheless, both models slightly overestimated the bias amplitude, most visibly in Fig. 8, where the models touched the edges of the noise bands. It is expected, therefore, that these models will generally improve P-OD state estimation performance in most cases, although not to the same level as the individual models.

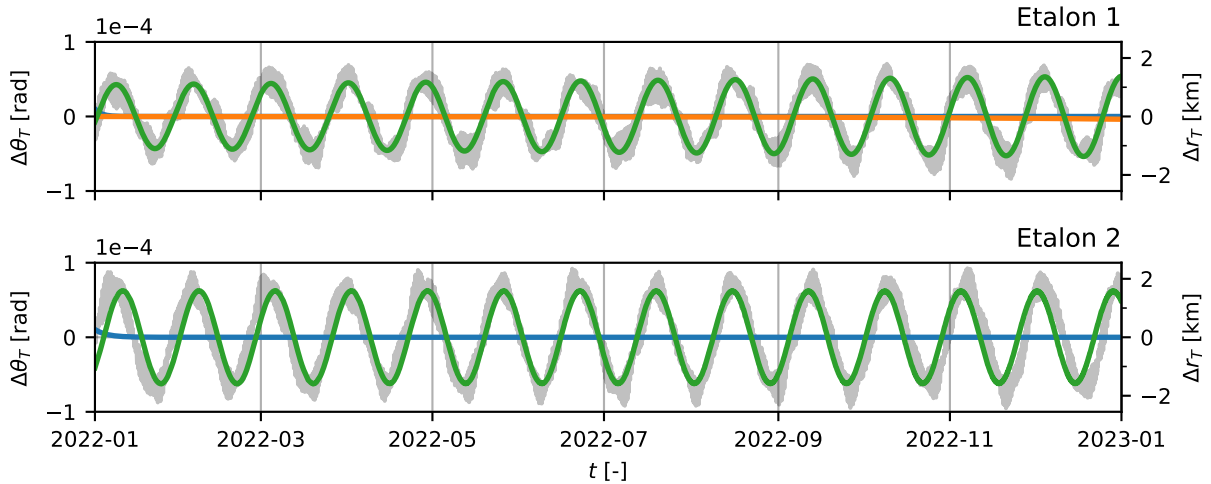


Fig. 6. Models for along-track error, using traditional DMD (blue), OptDMD (orange), and OptDMD with Hankel preprocessing (green). Note that, in the case of Etalon 2, OptDMD did not converge to a solution successfully. The Hankel preprocessing used 40 time delays, corresponding to two days of samples.

The difference in model performance between the LAGEOS and Etalon satellites might be a result of their different orbits. Etalon 1 and 2 lie in very similar orbits to the GNSS satellites, both in terms of semi-major axis and inclination. On the other hand, both LAGEOS satellites are in lower orbits at approximately half the altitude. Additionally, LAGEOS-1 lies in retrograde orbit with an inclination of approximately  $110^\circ$ . These cases, therefore, represent a high level of extrapolation for a model generated using only GNSS satellites.

## 5.2. GNSS Satellites

A comparison of the four models is presented in Fig. 9. The individual time- and moon-based models saw the most significant reduction in errors with typical RMSEs reducing by approximately 75% from 2000 m to 500 m. The mean position error was reduced by a similar amount. Additionally, the typical standard deviation in position error was reduced from approximately 1000 m to 250 m. The combined models were less effective at reducing RMSEs and mean errors with reductions of approximately 30% and 40% respectively. Nevertheless, these models were effective at halving the typical standard deviation to approximately 500 m.

Although the combined models had a limited impact on the position RMSE and mean position error, they had a major impact on the standard deviation, in both cases halving the typical value from approximately 1000 m to 500 m. In many cases, particularly with the GPS satellites, the TLEs of an individual satellite had a mean offset. In contrast, the combined models had a near-zero offset due to the averaging effect of including the residuals of a large set of satellites with various offsets about zero.

The combined models suppressed the periodic component of the along-track error but had a limited impact on the mean along-track error. This manifested as the reduction in along-track variation, resulting in a post-debiasing along-track error more closely representing a constant lead or lag, instead of an oscillation centred about the true state.

## 6. CONCLUSIONS

It has been shown that generalised models can be created which can be applied to large sets of satellites in the same orbital regime. Although not as effective as models tailored to each satellite individually, these models can reduce typical position errors and, importantly, suppress periodic variation in along-track error.

Nevertheless, even within a given regime, the behaviour of TLEs can vary between constellations, as observed in this study by differences in offset with Galileo and GPS satellites. It remains unclear as well how far these models can be extrapolated. For example, the LAGEOS satellites could not be debiased by the combined models successfully, likely due to their significant difference in semi-major axis and inclination.

This study was limited by its selection of satellites and corresponding data sources. The lack of available data for satellites and objects in a greater variety of orbits is a key blocker in the continuing development of bias correction models. One potential source of additional data is long-term P-OD on debris and rocket bodies to produce datasets approximating the true along-track errors present in TLEs [10]. Nonetheless, this is dependent on the further development of effective P-OD on TLEs.

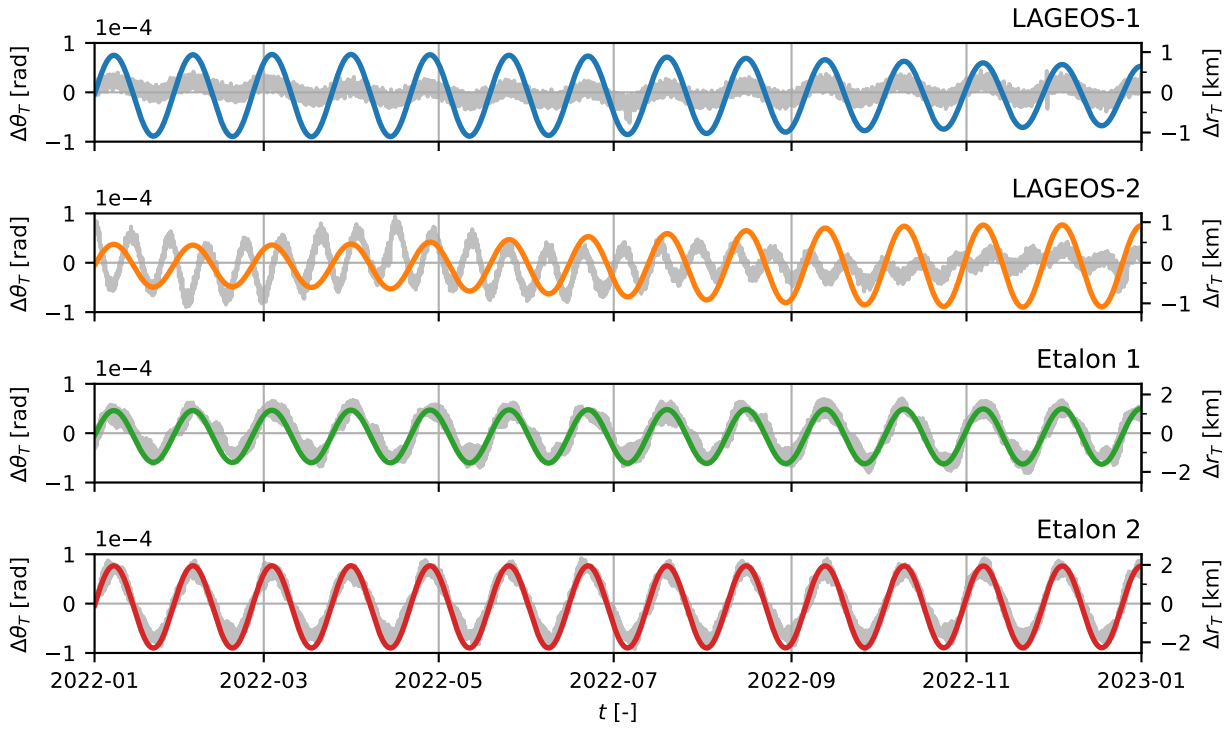


Fig. 7. Along-track errors of TLEs with respect to SLR. The SLR data and combined time-based models are presented in grey and colour respectively.

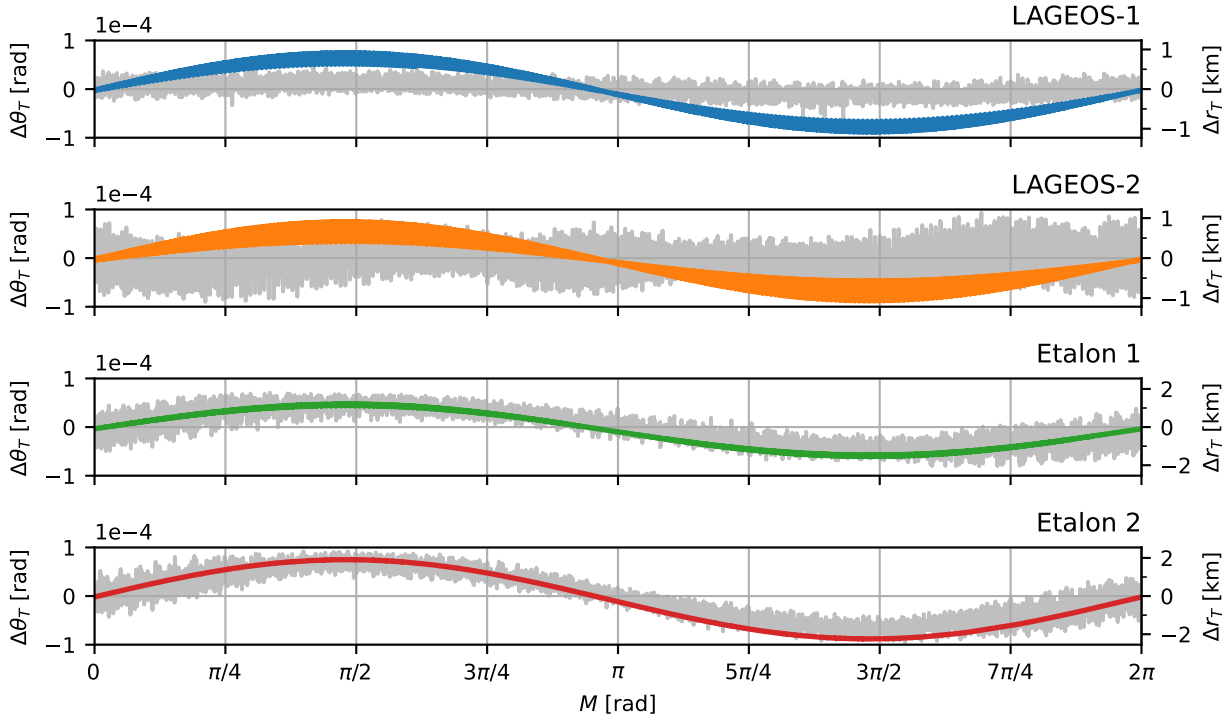
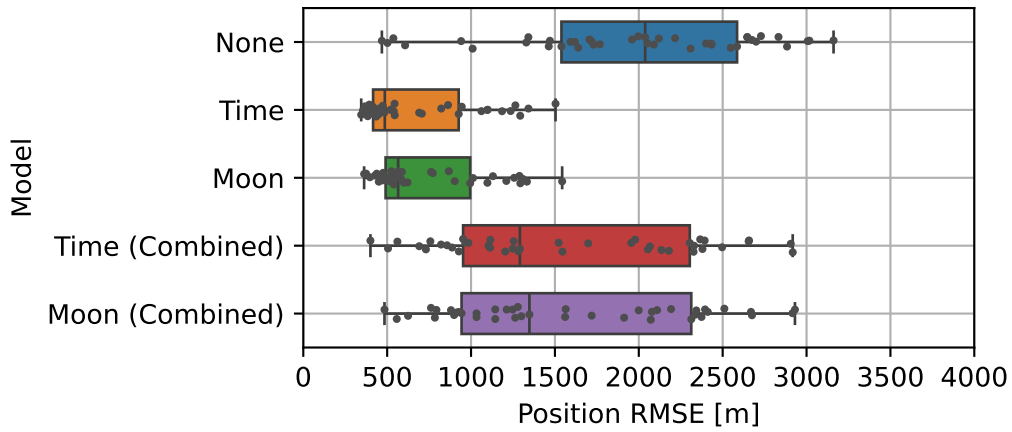
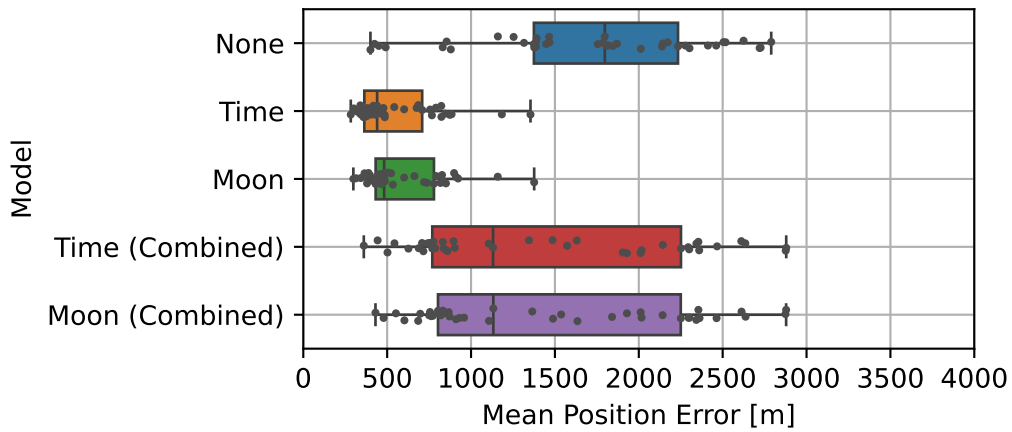


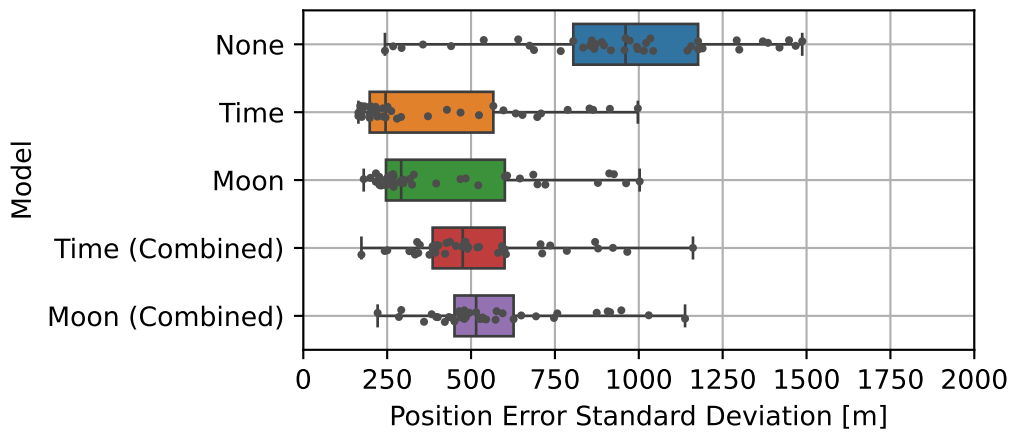
Fig. 8. Along-track errors of TLEs with respect to SLR. The SLR data and combined Moon-based models are presented in grey and colour respectively.



(a) Position RMSE.



(b) Mean position error.



(c) Position error standard deviation.

Fig. 9. Bias model performance for Galileo and GPS, evaluated over the entirety of the year 2022. Each dot represents the value of the metric for an individual GNSS satellite, while the coloured boxes indicate the quartiles of the distribution, and the whiskers the minimum and maximum values.

Ly, Lucken, and Giolito [9] noted that a longer-period component of along-track error existed due to mismodelling of the third-body perturbation from the Sun. Although a year-long variation should be observable within the current evaluation window, ideally a longer window should be used to capture multiple cycles. Future studies would benefit from extended windows to capture this behaviour.

The DMD-based models did not provide any advantages over the time-based model, but were subject to several limitations, notably sensitivity to hyperparameters and the input states. Although the method showed promise, particularly when considering the possibility of extending the method with additional states (such as radial and cross-track errors), it will require further investigation.

## 7. REFERENCES

- [1] “ESA’s Annual Space Environment Report,” ESA Space Debris Office, Darmstadt, Germany, 19th Jul. 2024. [Online]. Available: [https://www.sdo.esoc.esa.int/environment\\_report/Space\\_Environment\\_Report\\_latest.pdf](https://www.sdo.esoc.esa.int/environment_report/Space_Environment_Report_latest.pdf) (visited on 10/03/2025).
- [2] A. Holincheck and J. Cathell, “Improved Orbital Predictions using Pseudo Observations - Maximizing the Utility of SGP4-XP,” presented at the Advanced Maui Optical and Space Surveillance Technologies Conference, Maui, HI, USA, Sep. 2021.
- [3] D. Conkey and M. Zielinski, “Assessing Performance Characteristics of the SGP4-XP Propagation Algorithm,” presented at the Advanced Maui Optical and Space Surveillance Technologies Conference, Maui, HI, USA, Sep. 2022.
- [4] T. Payne, F. Hoots, A. Butkus, Z. Slatton and D. Nguyen, “Improvements to the SGP4 propagator (SGP4-XP),” presented at the Advanced Maui Optical and Space Surveillance Technologies Conference, Maui, HI, USA, Sep. 2022.
- [5] C. Levit and W. Marshall, “Improved orbit predictions using two-line elements,” *Advances in Space Research*, vol. 47, no. 7, 2011.
- [6] D. A. Vallado, B. Bastida Virgili and T. Flohrer, “Improved SSA through orbit determination of Two-Line-Element sets,” presented at the 6th European Conference on Space Debris, Darmstadt, Germany, April 2013.
- [7] J. Chen and C. Lin, “Research on Enhanced Orbit Prediction Techniques Utilizing Multiple Sets of Two-Line Element,” *Aerospace*, vol. 10, no. 6, 2023.
- [8] J. C. Bennett, J. Sang, C. Smith and K. Zhang, “Improving low-Earth orbit predictions using two-line element data with bias correction,” presented at the Advanced Maui Optical and Space Surveillance Technologies Conference, Maui, HI, USA, Sep. 2012.
- [9] D. Ly, R. Lucken and D. Giolito, “Correcting TLEs at epoch: Application to the GPS constellation,” *Journal of Space Safety Engineering*, Space Debris: The State of Art, vol. 7, no. 3, 2020.
- [10] M. I. Hallgarten La Casta and D. Amato, *Debiasing of Two-Line Element Sets for Batch Least Squares Pseudo-Orbit Determination in MEO and GEO*, 20th December 2024. [Online]. Available: <http://arxiv.org/abs/2412.15793> (visited on 10/03/2025), Accepted for publication in *Advances in Space Research*.
- [11] C.-C. Chao and F. R. Hoots, *Applied Orbit Perturbation and Maintenance*, 2nd ed. El Segundo, CA, USA: The Aerospace Press, 2018.
- [12] F. R. Hoots, P. W. Schumacher and R. A. Glover, “History of Analytical Orbit Modeling in the US Space Surveillance System,” *Journal of Guidance, Control, and Dynamics*, vol. 27, no. 2, 2004.
- [13] L. Maisonobe, V. Pommier and P. Parraud, “Orekit: an Open-source Library for Operational Flight Dynamics Applications,” presented at the 4th ICATT International Conference on Astrodynamics Tools and Techniques, Madrid, Spain, May 2010.
- [14] D. A. Vallado, *Fundamentals of Astrodynamics and Applications*, 4th ed. Hawthorne, CA, USA: Microcosm Press, 2013.
- [15] B. D. Tapley, B. E. Schutz and G. H. Born, *Statistical orbit determination*. Amsterdam, the Netherlands: Elsevier Academic Press, 2004.
- [16] K. Levenberg, “A Method for the Solution of Certain Non-Linear Problems in Least Squares,” *Quarterly of Applied Mathematics*, vol. 2, no. 2, 1944.
- [17] D. W. Marquardt, “An Algorithm for Least-Squares Estimation of Nonlinear Parameters,” *Journal of the Society for Industrial and Applied Mathematics*, vol. 11, no. 2, 1963.
- [18] J. N. Kutz, S. L. Brunton, B. W. Brunton and J. L. Proctor, *Dynamic Mode Decomposition* (Other Titles in Applied Mathematics). Society for Industrial and Applied Mathematics, 2016.
- [19] P. J. Schmid, “Dynamic mode decomposition of numerical and experimental data,” *Journal of Fluid Mechanics*, vol. 656, 2010.
- [20] J. H. Tu, C. W. Rowley, D. M. Luchtenburg, S. L. Brunton and J. N. Kutz, “On dynamic mode decomposition: Theory and applications,” *Journal of Computational Dynamics*, vol. 1, no. 2, 2014.
- [21] S. M. Hirsh, S. M. Ichinaga, S. L. Brunton, J. Nathan Kutz and B. W. Brunton, “Structured time-delay models for dynamical systems with connections to Frenet–Serret frame,” *Proceedings of the Royal Society A: Mathematical, Physical and Engineering Sciences*, vol. 477, no. 2254, 2021.

- [22] T. Askham and J. N. Kutz, "Variable Projection Methods for an Optimized Dynamic Mode Decomposition," *SIAM Journal on Applied Dynamical Systems*, vol. 17, no. 1, 2018.
- [23] D. Sashidhar and J. N. Kutz, "Bagging, optimized dynamic mode decomposition (BOP-DMD) for robust, stable forecasting with spatial and temporal uncertainty-quantification," *Philosophical Transactions of the Royal Society A: Mathematical, Physical and Engineering Sciences*, vol. 380, no. 2229, 2022.